Tellus (1987), *39A*, 334–353

Numerical simulations of polar lows in the Norwegian Sea

By S. GRØNÅS, A. FOSS and M. LYSTAD, *The Norwegian Meteorological Institute, P.O. Box 320, Blindern, N-0314 Oslo 3, Norway*

(Manuscript received 24 June 1986; in final form 13 January 1987)

ABSTRACT

A high resolution version of an operational weather prediction model has been developed. An explicit time integration scheme is used on a limited area polar stereographic grid. The physical parameterization of surface fluxes, fluxes in the free atmosphere, stratiform and convective precipitation are relatively simple and no radiation processes are involved. Simulations are presented for six synoptic situations when polar lows occurred in The Norwegian Sea. Analyses from the European Centre for Medium Range Weather Forecasts (ECMWF) are used as initial analyses. The simulations are verified against published subjective analyses. In one case, analyses from detailed aircraft measurements were available.

In most cases the horizontal grid distance has been 50 km; in one case 25 km resolution was used. The integrations started before any polar low was observed and lasted for 36 or 48 hours. The model creates polar low disturbances at approximately the right position at the right time. The predicted intensity is, however, generally too weak.

All the simulated polar lows show an initial phase where a baroclinic development takes place in a reversed shear flow. Usually the structure is relatively shallow. The low-level trough or low is found to be warm, and conditional vertical instability is connected to it. In this way, a synoptic situation is prepared which is favourable for some CISK-like mechanism which sometimes further develop the polar low. The model does not handle this rapid growth properly, probably due to lack of resolution or incomplete parameterization of convection.

In all cases, cross-sections perpendicular to the trough-like disturbance show a warm occlusion, or a double-front system. The front also exists when precipitation processes are excluded in the model; however, release of latent heat strengthens the vertical circulations generally connected to each branch of the occlusion. A rapid development of a polar low might be connected to locally descending air in between the two circulations; satellite pictures indeed show a cloud-free eye in some cases.

1. Introduction

The development of polar lows has been studied by several authors. Harrold and Browning (1969) concluded that the polar low is purely baroclinic in origin. This was supported by Mansfield (1974) and Duncan (1977). Duncan (1978) pointed out that the baroclinic development often takes place in a reversed shear flow (surface wind and thermal wind in opposite direction). Other investigators suggest CISK (Conditional Instability of Second Kind) as the primary growth mechanism for polar lows (Rasmussen, 1979, 1981; Økland, 1977). Bratseth (1985) reconsidered the possibility of CISK in a simple analytical model. His results indicate that CISK in polar air masses is possible if the heating takes place in a shallow layer at low levels. Sardie and Warner (1983) studied the relative importance of baroclinicity and CISK. Sardie and Warner (1985) also simulated a Pacific and an Atlantic polar low. For the Atlantic low (maximum vorticity close to the Coriolis parameter), baroclinicity was the dominant mechanism during the first 24 hours of the simulation. Release of latent heat played a significant role in the intensification during the last 24 hours of the 48-hour simulation.

The aim of the present paper is to investigate the potential of a high-resolution numerical model to simulate polar lows over the Norwegian Sea. So far only a few numerical simulations based on observations have appeared in the literature. Seaman et al. (1982) integrated the Pennsylvania State University mesoscale model with 50 km horizontal resolution (for a description of the model see Anthes and Warner, 1978) to predict the development of a polar low in the North Sea. In their simulations, the low was present in the initial analysis. In the study by Sardie and Warner (1985), the same model was used with a horizontal resolution of 80 km. They started the integration before the low was formed and verified against conventional analyses.

At the Norwegian Meteorological Institute (NMI), a project on polar lows was carried out in 1983–85. A map of the investigated area is shown in Fig. 1. In this connection, a high-resolution version of the operational Norwegian limited area model was developed. The model was later made operational with a horizontal resolution of 50 km (Grønås and Midbø, 1986; Nordeng, 1986). The hydrostatic model was used for several simulations of polar lows in the Norwegian Sea. All integrations started from ECMWF analyses at a time when no sign of a polar low was present.

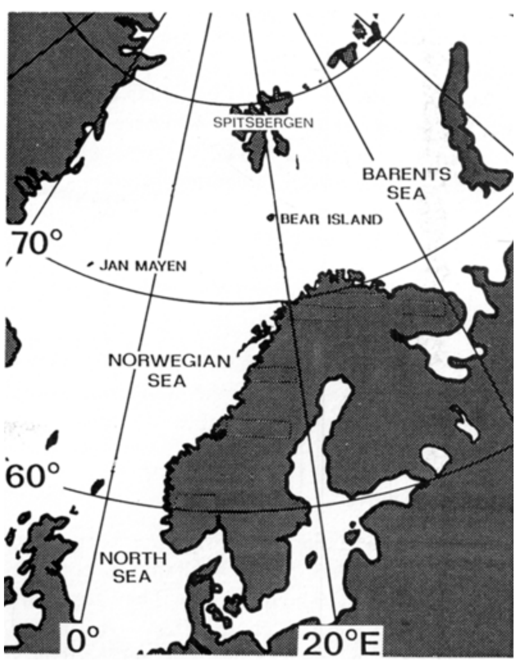

Fig. 1. Investigated area during the Polar Lows Project.

The main objective has been to simulate the life cycle of the polar lows and to study the potential of our model to predict the development. The result has been verified against reanalysed subjective analyses published during the project. Conventional observations, a network of drifting buoys, and satellite pictures from polar orbiting satellites were used. In one of the cases, 27 February, 1984, the NOAA Arctic Cyclone Expedition made detailed measurements from a research aircraft of a polar low southeast of Jan Mayen (Shapiro et al., 1987).

2. The limited area prediction model

A short description of the model is given below. It is a version of the operational NWP model of the Norwegian Meteorological Institute. A more detailed description can be found in Grønås and Hellevik (1982).

2.1. General formulations

The horizontal grid is a polar stereographic grid, true at 60° N. The vertical coordinate is a generalized σ-coordinate defined by

$$\sigma = (p - p_t)/(p_s - p_t),$$

where p_s is the pressure at the earth's surface, and p_t the pressure at the top of the model atmosphere. Independent variables are: x, y, σ, t, where x, y are the horizontal coordinates and t is time. Dependent variables are: u, v, θ, q, p_s, where u and v are horizontal wind components, θ, potential temperature and q specific humidity. Diagnostic variables are ϕ and $\dot{\sigma}$. The hydrostatic relation is $\partial\phi/\partial p = -\pi\phi$, where π is the Exner function.

The integration domain is a rectangle on the polar stereographic projection map. The resolution can be varied both in the horizontal and in the vertical. In the experiments described here, we used 10 vertical levels and 61 × 49 grid points at each level. Polar stereographic coordinates are very convenient in limited-area models when the integration area covers the pole or is close to the pole. However, if the area is large, the real grid distance will be significantly smaller in the southern than in northern areas.

The grid shown in Fig. 2 is the Arakawa *D*-grid combined with staggered sigma layers. One

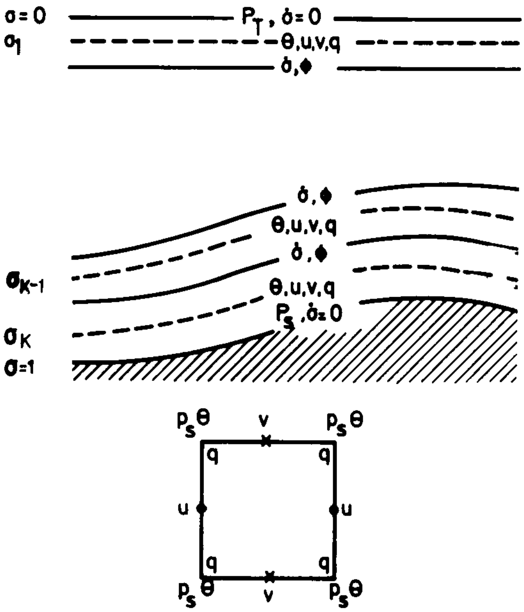

Fig. 2. Distribution of the model variables in the horizontal (lower) and vertical (upper) direction.

advantage of the D-grid is that no spatial averages are involved in computing the Coriolis term. Mesinger and Arakawa (1976) considered the D-grid to be inadequate for the simulation of gravity-inertia waves. However, our special time integration method will remove these difficulties. The staggered sigma layers (see Fig. 2) ensure a hydrostatically consistent formulation of the pressure term (Janjic, 1977).

The explicit time integration is formulated according to Bratseth (1983). Second-order accurate tendencies are first computed at the centres of the grid squares, and then interpolated to the positions where the corresponding variables are defined by the following formula:

$$\langle\alpha\rangle_{xy} = \langle\langle\alpha\rangle_x\rangle_y, \qquad (1)$$

where

$$\langle\alpha\rangle_x = (1 + A)(\alpha(x + d/2) + \alpha(x - d/2))/2$$
$$-A(\alpha(x + 3d/2) + \alpha(x - 3d/2))/2.$$

For $A = \frac{1}{8}$, which is the standard value used in the model, this interpolation method is correct to 4th order in d. For this value, the time step could be nearly doubled compared to the time-staggered scheme. It has been shown by Bratseth (1983) that the accuracy is virtually unchanged except for very short waves. He also found that nonlinear instability is a much smaller problem in our scheme than in time-staggered schemes. Because of this, there is no explicit horizontal diffusion in the model. Since our scheme is not time-staggered, the so-called Schuman pressure gradient averaging technique, which again almost doubles the maximum time step, can be applied. We have adopted this method as described by Brown and Campana (1978) and the required parameters are as given in their paper. In our explicit integration method, a time step of 450 s is used in the operational model when the grid distance is 150 km at 60° N. By reducing the accuracy in the interpolation formula (1) south of 40° N, the time step in the operational model is further increased.

We separate between 4 types of surface and surface drag: ocean, ice, unspecified land and forest. The roughness parameter is constant over oceans. There is no additional drag in mountainous areas and no attempt to correct for a reflecting upper boundary. The sea surface temperature (SST) must be specified. The orography is constructed in a subjective way. For Europe (Greenland included), contours of valley-filled envelope mountains have been drawn from atlas maps.

At the lateral boundaries, the relaxation method of Davies (1976) and Kållberg (1977) is used. Let α_m denote a model variable and α_r a variable from a model integrated in advance on a hemispheric or a global area. The relaxation procedure is then written:

$$\alpha = (1 - \gamma)\alpha_m + \gamma\alpha_r. \qquad (2)$$

If N denotes the width in number of grid points of the boundary zone, and n the number of points from the boundary, then within the zone, γ is defined as:

$$\gamma = ((N - n)/N)^2. \qquad (3)$$

We use $N = 6$ in our model. In our experiments, the boundary values α_r are available in pressure coordinates every 6 hours or less. They are interpolated to sigma coordinates. A linear interpolation in time is used to get boundary values every time step.

2.2 Parameterization of subgridscale processes

The parameterization of physical processes is rather simple and does not include radiation. We give here a brief description of how the subgridscale processes are parameterized

2.2.1. Surface fluxes. Let α denote momentum, heat or humidity and τ_α the vertical flux of α, then

$$\frac{\partial \alpha}{\partial t} = \frac{1}{\rho}\frac{\partial \tau_\alpha}{\partial z} = \frac{g}{(p_s - p_t)}\frac{\partial \tau_\alpha}{\partial \sigma}. \tag{4}$$

The surface fluxes of momentum τ_v, heat τ_θ, and humidity τ_q, respectively, are computed as follows:

$$\tau_v = \rho F_v(\mathrm{Ri}, z_0)\,\mathbf{v}, \tag{5}$$

$$\tau_\theta = -c_p\,\rho F_\theta(\mathrm{Ri}, z_0)\,(T_s - T_h) \simeq -\pi_h\,\rho F_\theta(\mathrm{Ri}, z_0)\,(\theta_s - \theta_h), \tag{6}$$

$$\tau_q = -L\rho F_\theta(\mathrm{Ri}, z_0)\,(q_{sat}(T_s, p_s) - q_h). \tag{7}$$

Here, s denotes the surface and h the lowest sigma layer. The functions F_v and F_θ are defined as by Louis (1979). Our definition of the Richardsons number is:

$$\mathrm{Ri} = gh_s(\theta_h - \theta_s)/(\theta_h |V_h|^2). \tag{8}$$

Here, h_s is the height of the lowest sigma layer, θ_h is the potential temperature and V_h the wind vector at that level. In the model version used in our experiments, there are no fluxes of heat and moisture from land and ice surfaces.

2.2.2. Fluxes in the free atmosphere. Vertical fluxes in the free atmosphere are computed with the dry-adiabatic adjustment method. Let k denote an index of the model layers (increasing downwards). In a stable atmosphere, when $\theta_k > \theta_{k+1}$, the vertical flux is put equal to zero.

In an unstable atmosphere, when $\theta_k < \theta_{k+1}$, we introduce a full adjustment to neutral conditions within one time step. This gives the following relation to compute an exchange coefficient K for fluxes of moisture and momentum:

$$2\Delta t g/(p_s - p_t)\,\tau_\alpha = K(\alpha_k - \alpha_{k+1}), \tag{9}$$

then we have

$$K = \Delta\sigma_k\,\Delta\sigma_{k+1}/(\Delta\sigma_k + \Delta\sigma_{k+1}), \tag{10}$$

where $\Delta\sigma_k = \sigma_{k+\frac{1}{2}} - \sigma_{k-\frac{1}{2}}$.

2.2.3. Condensation and precipitation. Condensation occurs in the model when $q_k > q_{sat}$, and then clouds and precipitation are computed as follows. First, the possibility of conditional instability is tested. A convective cloud with moist-adiabatic temperature lapse rate is constructed with base at level $k_{base} = k$. Here we have $q_{ck} = q_{sat}(T_{ck}, p_k)$, where $T_{ck} = T_k$. The temperature at higher levels (lower value of k) is given by

$$T_{ck-1} = T_{ck} + (\partial T/\partial p)_k(p_{k-1} - p_k), \tag{11}$$

where $\partial T/\partial p$ is given by the moist-adiabatic lapse rate. If $T_{ck-1} > T_{k-1}$, no convection is found and a layer cloud is defined at level k. If $T_{ck-1} < T_{k-1}$, a convective cloud is defined. The top of the cloud is at level $k - 1$ or at a higher level. The computations above are repeated for higher levels to find the top of the cloud k_{top}.

Within the convective clouds, new values of temperature and humidity are computed from the following formulas.

$$T' = (1 - a)\,T + aT_c = T + a(T_c - T), \tag{12}$$

$$q' = (1 - a)\,q + aq_c = q + a(q_c - q). \tag{13}$$

Here,

$$a = ((q_{base} - q_{sat})\,\Delta\sigma_{kbase})/(\sum_k (q_{ck} - q_k + c_p/L(T_{ck} - T_k))\,\Delta\sigma_k),$$

$$q = q_{kbase} = q_{sat}.$$

In case of layer clouds, the heat of condensation is added at level k. The new temperature and humidity are given by

$$T' = T + \Delta T = T - L/c_p\,\Delta q, \tag{14}$$

$$q' = q + \Delta q = q_{sat}(T', p) \approx q_{sat}(T, p) + \partial q_{sat}/\partial T(\Delta T) = q_{sat}(T, p) - (\varepsilon L/c_p\,T)(L/RT)\,q_{sat}\,\Delta q. \tag{15}$$

This gives

$$\Delta q = (q_{sat}(T, p) - q)/(1 + (\varepsilon L/c_p\,T)(L/RT)\,q_{sat}). \tag{16}$$

Preciptation is computed from the total heat of condensation. No evaporation of precipitation is included. If convection occurs, no large-scale (stratiform) precipitation is computed. When no convection occurs, large-scale condensation is computed.

2.3. *Initialization*

The iterative dynamical method proposed by Bratseth (1982) has been implemented. The model equations are integrated two time steps to get second-time derivatives of the variables.

If F_i^n denotes the state of the model at iteration n and time step i, then

$$\partial^2/\partial t^2(F) \sim F_2 + F_0 - 2F_1 = Z_1. \tag{17}$$

The iteration is completed by

$$F^{(n+1)} = F^{(n)} + \Gamma Z^{(n)}. \tag{18}$$

Here Γ is a linear operator which has to be chosen so that synoptic scale modes are mainly unaltered and gravity-inertia modes are damped.

The ideal choice for Γ is an operator which has the normal modes of the model as eigenvectors. Then the meteorological modes could be left unchanged and the others removed.

We have chosen a much simpler operator which decomposes into two vertical parts and five horizontal wave packages. If Z_{vh} denotes a wave package with vertical structure v and horizontal structure h, then

$$Z = \sum_{v,h} Z_{vh}, \tag{19}$$

$$\Gamma Z = \sum_{v,h} \gamma_{vh} Z_{vh}, \tag{20}$$

where γ_{vh} is the damping that has to be chosen for the corresponding wave package Z_{vh}.

Horizontally the quantity Z is decomposed in wave packages derived by use of a smoothing formula applied on different scales. Vertically, we have one barotropic part defined by a vertical average and one baroclinic part which is the deviation from the barotropic part.

The constants γ_{vh} are chosen in order to obtain fast covergence for a wide range of horizontal wave lengths without risking instability for high-frequency waves. The constants are estimated from the formula for the frequency of a model gravity mode. The choice is model-dependent and our values may not work well in other models with different dispersion relations. The operator is modified near the boundaries.

In our experiments, 3 iterations ensure an efficient damping of the gravity waves (Fig. 3). The maximum corrections of the surface pressure due to the initialization are of the order 1 hPa in the high-resolution model versions applied.

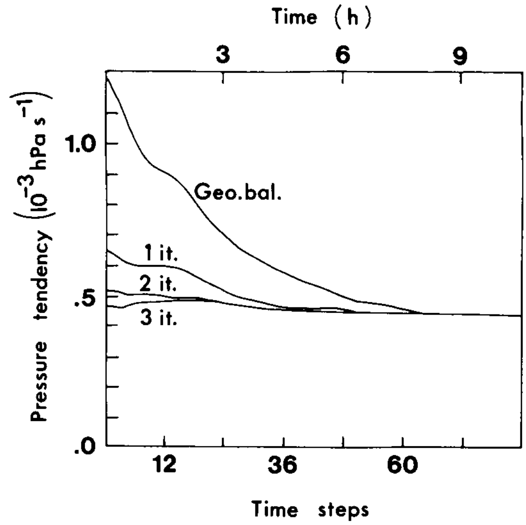

Fig. 3. Damping of gravity waves by our initialization method. The curves show the variation with time of the area mean absolute value of the surface pressure tendency. The upper curve shows the damping from an initial state in geostrophic balance. The other curves show the damping when 1, 2 and 3 iterations are used.

3. The design of the experiments

For our experiments, we have used initialized analyses of wind components, height and specific humidity in pressure coordinates from the ECMWF operational analyses. The horizontal resolution is 1.875 degrees in latitude and longitude, and data from 1000, 850, 700, 500, 400, 300, 200, 100 hPa surfaces were used. The analyses were interpolated to the integration areas used by our model. A second-order interpolation scheme was used. The pressure analyses were then interpolated to model sigma coordinates by linear interpolation in the Exner function.

Altogether the model was run on 3 integration areas (see Fig. 4a), which all contain the same number (61 × 49) of horizontal grid-points. The first and largest area is equal to that used operationally at the Norwegian Meteorological Institute, which covers North Atlantic, Europe, and part of North America. The grid distance is

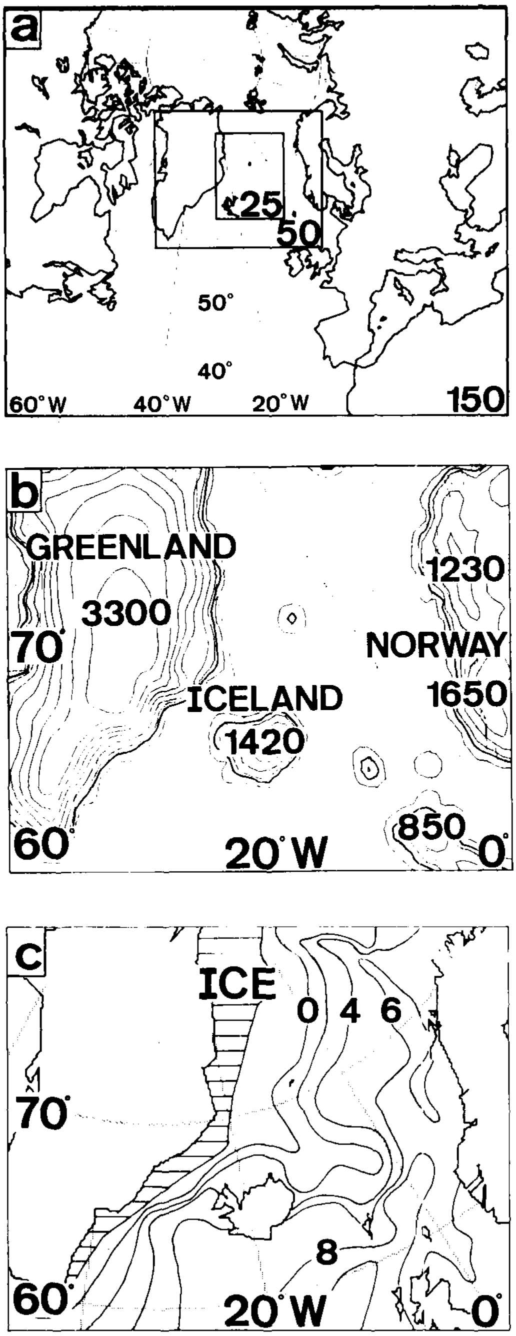

Fig. 4. (a) Areas of integration of the numerical model with 3 different grid sizes: 150 km, 50 km, 25 km. The two inner areas are moveable. (b) Height contours of the orography (m) used in the 50 km grid model. (c) Ice border and sea surface temperature (°C) used in the simulations.

here 150 km at 60° N and the lateral boundary values of all the simulations were interpolated from the ECMWF analyses. The second area has 50 km horizontal resolution. The location of this area has been varied from case to case and centred around the disturbance to be simulated. One such area is shown in Fig. 4b together with the orography. The lateral boundary values in some experiments were given from integrations in the larger area. In other experiments, the boundary values were interpolated from the ECMWF analyses. The time interval of the boundary values was 6 hours for both kinds of nesting. In the third and smallest area, the grid distance has been 25 km and it is located inside the second area. Initial conditions have been a prediction from the second area. Results every 3 hours from the 50 km area were used as lateral boundary values.

In all experiments, 10 vertical sigma levels were used. As the horizontal resolution is increased, the top level is lowered and the number of sigma levels increased below 700 hPa. The sigma levels in the different model versions are given in Table 1. The position of the ice edge and the sea surface temperature (SST) are taken from the actual operational maps produced by the Norwegian Meteorological Institute (see, Fig. 4c).

We will mainly present the results of the integrations in pressure coordinates. The interpolation from sigma to pressure coordinates is again linear in the Exner function. Above mountains, little care is paid to the extrapolation of variables to the 1000 hPa surface. For wind and temperature, the values in the lowest sigma layer (see Table 1) are presented. The results are stored every third hour. Since our model contains some noise with wavelength equal to two grid distances, reflected from the boundaries, a second-order Shapiro filter (Shapiro, 1970) is applied to the output fields. The vertical cross sections are computed from results in sigma levels directly. The pressure vertical velocity fields are not smoothed in time.

The model has been integrated without explicit horizontal diffusion. For integrations with 25 km resolution, a fourth-order Shapiro filter has been applied for smoothing of the dependent variables every six hours to prevent a kind of nonlinear instability which might occur. This instability

Table 1. *Position of sigma surfaces when p_s = 1000 hPa*

Level	150 km p_t = 100		50 km p_t = 200		25 km p_t = 300	
k	σ	p(σ)	σ	p(σ)	σ	p(σ)
1	0.05	145	0.094	275	0.094	357
2	0.15	235	0.225	380	0.225	457
3	0.25	325	0.450	560	0.450	615
4	0.35	415	0.600	680	0.600	720
5	0.45	505	0.713	770	0.713	798
6	0.55	595	0.775	820	0.775	842
7	0.65	685	0.825	860	0.825	877
8	0.75	775	0.875	900	0.875	912
9	0.85	865	0.925	940	0.925	947
10	0.95	955	0.975	980	0.975	982

Table 2. *The basic experiments*

Initial analysis	Hours of integration	Horizontal mesh
2 Dec 1981 12 GMT	48	50 km
15 Dec 1982 12 GMT	48	50 km
19 Dec 1983 12 GMT	36	50 km
26 Feb 1984 00 GMT	48	50 km, 25 km
29 Feb 1984 12 GMT	36	50 km
5 Mar 1984 12 GMT	36	50 km

sometimes appears when integrations are started from analyses interpolated directly from pressure to sigma coordinates. The interpolations might give artificial warm cores above the mountains, which in turn might cause overdevelopments when the air is advected from the mountain tops.

The initial time of the integrations has usually been 24 hours prior to the time when the polar low or family of lows was first observed. The total time of integration has been 36 or 48 hours. Altogether, 6 cases have been simulated. The initial time and the length of the integrations are given in Table 2. For each situation, a control experiment with a horizontal resolution of 50 km has been made. In these experiments, all the physical effects were included as described in Section 2 and the lateral boundary values were taken from an integration on the largest area (150 km resolution). For some situations, many sensitivity experiments with respect to boundary values, horizontal resolution, and physical processes were made.

4. The synoptic situations

The synoptic situations are chosen from a list of polar lows reported by Wilhelmsen (1985, 1986), and Kristoffersen (1985). In connection with the Polar Low Project, some of these cases have been reanalysed (Hoem et al., 1984; Hoem, 1985; Hoem and Hoppestad, 1986; Rabbe, 1987; Rasmussen, 1985). Of the six situations investigated in this paper, 4 are discussed in these articles.

In all cases, the polar lows are found in the Norwegian Sea west of the Norwegian coast and west of a line from Spitsbergen to North Norway. The situations are dominated by synoptic-scale cyclones crossing the Norwegian Sea from west. In the rear of these cyclones, northerly surface winds are present which advect colder air above the ice toward the sea. The polar lows are formed in this cold flow over the ocean. In some cases, the synoptic scale lows have a large scale and the distance from the centre to the area where the polar lows are formed is relatively large. In other situations, the synoptic scale lows are weaker, and the formation area of the polar lows is closer and often connected to the occlusion of the synoptic-scale cyclone. In Figs. 5a, b, the ECMWF initial 1000 hPa height and potential temperature analyses are shown from 2 of the situations.

In all cases, a core of cold air is present above the ice east of Greenland; surface temperatures of −20°C or below are found here. There are large horizontal temperature gradients in the

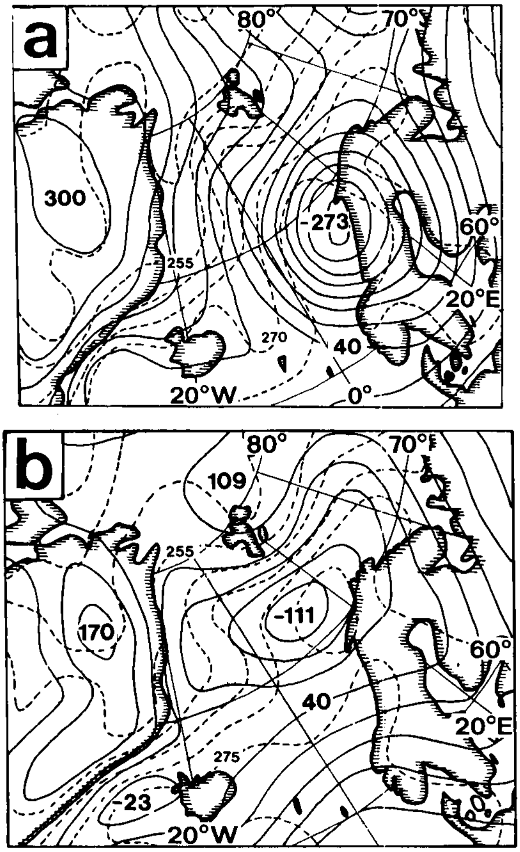

Fig. 5. ECMWF 1000 hPa (solid contours, interval 40 m) height and potential temperature (dashed contours, interval 5 K) analyses. (a) 12 GMT 29 February 1984. (b) 12 GMT 5 March 1984.

boundary layer toward the open, warm sea. Differences of 15–25°C within distances of approximately 400 km are found. The cold core is noticeable at 850 hPa, but the temperature differences are reduced to approximately 5°C. At 700 hPa, the temperature differences across the ice edge are small or negligible.

In both cases presented in Fig. 5, and also in 3 other cases, the initial analyses show a remarkable tongue of warm air in the boundary layer southwest of Spitsbergen. The formation of the polar lows in our cases is connected to these warm, shallow structures. The warm tongue is probably formed by differential heating connected to the similar warm tongue of sea-surface water found in the area (see Fig. 4c). The edge of the ice also has a shape like a tongue, or a triangle north of Bear Island. In the first example (Fig. 5a), the flow was northerly for 24 hours prior to the time of the analysis. Cold air is advected along the ice both east of North Greenland and east of Spitsbergen. Northerly winds also prevail over the open tongue and here the air is efficiently heated from below. Such heating has been studied by Økland (1976). He also studied the formation of fronts along an ice edge (Økland, 1978). Because of lee effects, the northerly winds tend to become weaker southwest of Spitsbergen than in the surroundings. Northerly winds crossing the Spitsbergen mountains will be stronger on the eastern side. In addition, weak and stable flows will often be blocked by the mountains and steered around on the eastern side. Such effects might strengthen the deformation of the flow.

In the other example, Fig. 5b, the warm tongue is connected with an occlusion north of the synoptic scale cyclone. It is often found that the polar low is formed on the occlusion in the rear of the synoptic-scale cyclone. Processes like those mentioned above might strengthen the occlusion, or warm tongue in the boundary layer.

5. Results

There is a large difference in the resolution of the ECMWF analyses and the resolution of our mesoscale model. During the first 6–12 hours of the integrations with 50 km resolution, an adjustment takes place from the initial conditions toward the model mesoscale solutions. During this period, strong shallow fronts are formed over the Norwegian Sea. An example is found on the western side of the cross-section in Fig. 7. Temperature differences of more than 5°C within 100 km are often found. While initial maximum vorticity at the surface is generally below 0.5 times the Coriolis parameter f, vorticity of 2 and $3f$ is often found along the surface fronts after 12 hours of itegration. The depth of the fronts is usually less than the height of the 700 hPa surface. The production of vorticity is connected to strong vertical circulations at the front. Upward vertical velocities close to 0.5 ms^{-1} are found together with precipitation amounts of 1–4 mm/3 hours. The initial analyses contain sufficiently strong temperature gradients to force vertical circulations in the model. In turn, they intensify the gradients and tend to create a discontinuity. This is in accordance with theory on fronts (Hoskins and Bretherton, 1972). However, the resolution of the model puts a limit to how far this frontal process can be developed.

Assimilation of observations in the model for a period prior to the start will remove much of the adjustment process, and simplify the discussion of the mesoscale simulations.

5.1. Baroclinic development in a reversed shear flow

In all our simulations, there are baroclinic developments present which form the polar low or make a synoptic situation favourable for CISK-like mechanisms to further develop the low. Investigations on the growth of baroclinic waves are generally dealing with occasions when the thermal wind and the progression of the disturbance are in the same direction. In our cases, the baroclinic instability takes place in a reversed shear flow. The wind at the steering level is northerly and in the opposite direction to the thermal wind. The growing disturbance will form a low-level trough and a more closed circulation aloft. The vertical tilt of the disturbances is foreward along the low-level flow. Duncan (1978) described baroclinic development in a reversed flow with a simple, quasi-geostrophic model. The surface winds are stronger than in ordinary unreversed occasions and Duncan concluded that the disturbances are more likely to develop over water surfaces where frictional damping is reduced. Haugen (1986) studied baroclinic growth in a reversed flow typical for one of our situations. An adiabatic, primitive equation model with cyclic boundary conditions in the north-south direction was used. A warm surface trough was formed, and conditional vertical instability was found.

5.1.1. 15–17 December 1982. This situation is an example of a baroclinic development in a reversed shear flow. A very deep low is crossing Scandinavia eastward. At the time of the initial analyses (12 GMT 15 December), strong winds prevail over the Norwegian Sea. In the lower layers, a cold core is found east of Greenland. There exist pronounced temperature gradients across the ice edge, and a warm tongue southwest of Spitsbergen.

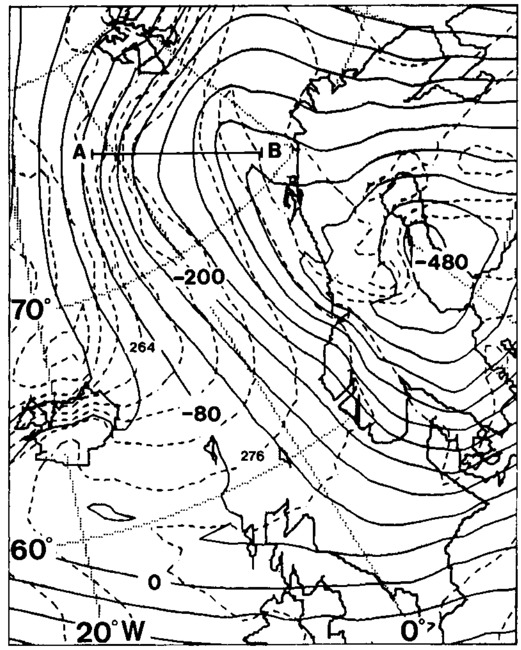

Fig. 6. Prediction of 1000 hPa height and potential temperature (dashed contours, interval 3 K) at the lowest sigma level. 12 GMT 15 December 1982 + 24 hours.

Fig. 6 shows a 24-hour prediction of 1000 hPa height and potential temperature at the lowest sigma level. The cold air east of Greenland still moves southward and the low-level frontal struc-

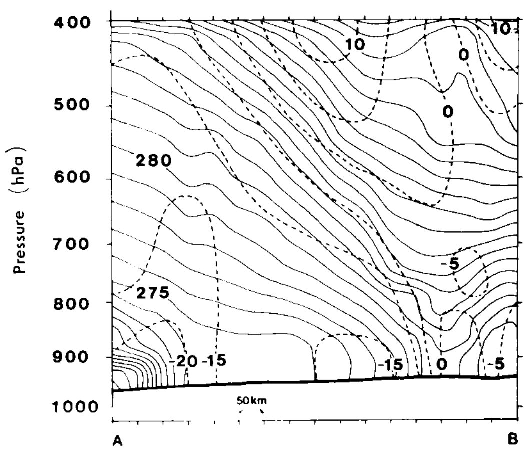

Fig. 7. Cross-section of potential temperature (solid lines, interval 1 K) and normal wind velocity (dashed lines, interval 5 ms^{-1}) (northerly wind negative). For position see Fig. 6.

ture southwest of Spitsbergen is strengthened. A lee trough has formed west of North Norway and is moving westward. The deep baroclinicity is connected to this trough as shown in the cross-section, Fig. 7. The reversed flow is clearly demonstrated, and we also see the shallow structure of the front southwest of Spitsbergen. We note the warm, funnel-shaped occlusion above the trough. Similar structures are found in connection with all disturbances which in our simulations are associated with polar lows. Conditional instability exists within the occlusion.

During the next 24 hours of the integrations, the trough turns southward into the shallow front and then moves southward. The 48-hour forecasts at 1000 and 500 hPa are shown in Figs. 8a, b. There are now strong surface winds west of the warm surface trough. At 500 hPa, the disturbance is more circular and the tilt of the height disturbance is southeastward from the surface. This is also in agreement with the results found by Haugen. (1986). We notice a smaller-scaled temperature wave near the surface in the middle of the trough, within the larger-scaled temperature wave connected with the deep baroclinic disturbance. This indicates the existence of an additional smaller-scale baroclinic disturbance on the shallow front.

The verifying analysis from Hoem et al. (1984) is found in Fig. 9 and a satellite picture some hours earlier in Fig. 10. Our prediction seems to be approximately 6 hours too slow, but otherwise reasonably accurate. The minimum surface pressure in the analysis is approximately 5 hPa deeper and a closed circulation is indicated. The model precipitation (not shown) is in a band northward from the trough and seems to be in agreement with the satellite picture. When ECMWF analyses are used as lateral boundary values, the positioning of the low is much better. When precipitation processes are excluded in the model and there are no heat fluxes from the ocean, the deepening of the low is approximately 5 hPa less.

5.1.2. 5–7 March 1984. The initial state at 1000 hPa is shown in Fig. 5b. During the first 6–12 hours of the integration, the occlusion is strengthened, precipitation is found in a band far westward and vorticity is increased to between 3 and $4f$. The occlusion turns southward and interacts with a deeper baroclinic disturbance. After

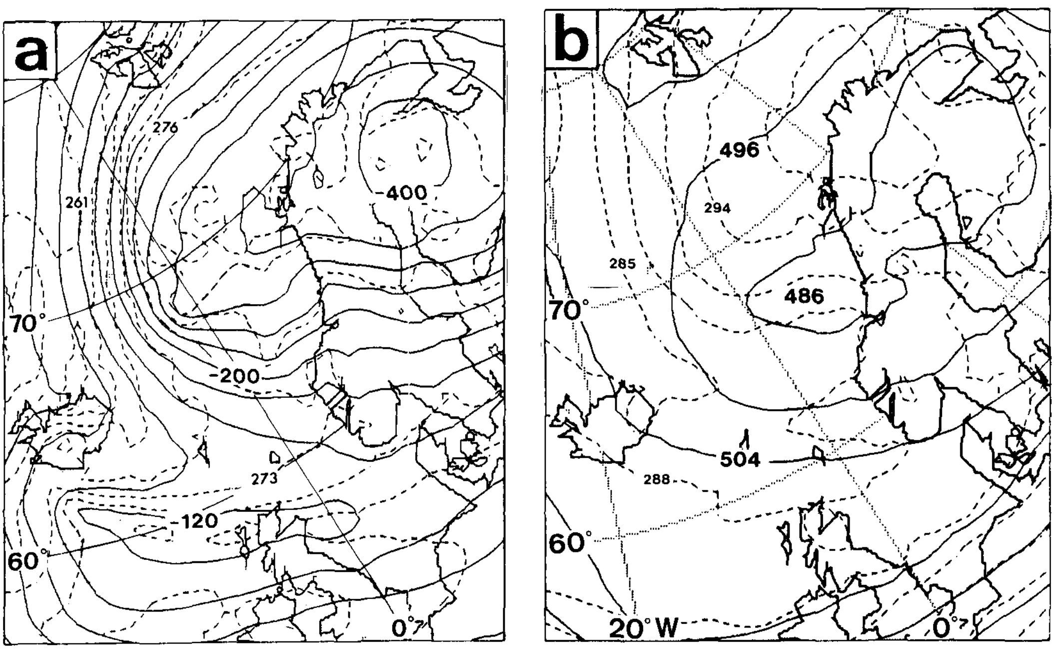

Fig. 8. Prediction 12 GMT 15 December 1982 + 48 hours. (a) 1000 hPa height and potential temperature (dashed lines, interval 3 K) at the lowest sigma level. (b) 500 hPa height (interval 8 decameters) and potential temperature (interval 3 K).

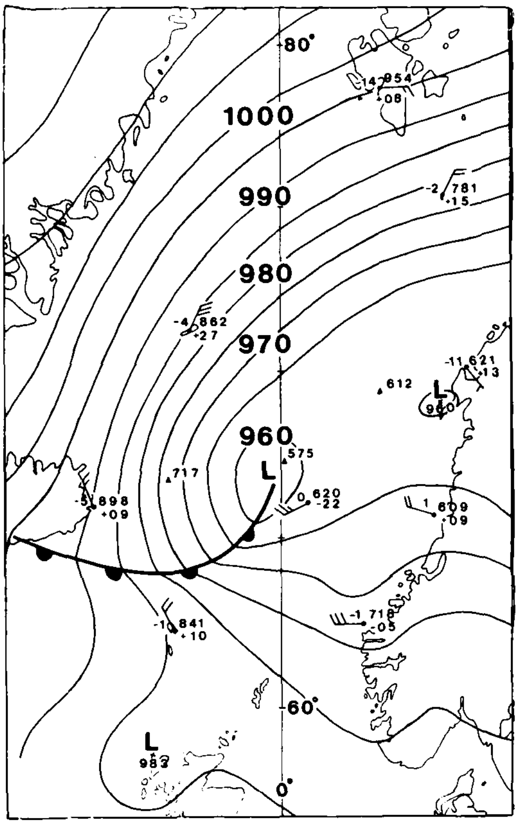

Fig. 9. Surface analysis 12 GMT 17 December 1982 (Hoem et al., 1984).

24 hours, a surface low is present, the disturbance is deep and the tilt is southward. The predicted wind in the lowest sigma layer after 36 hours is shown in Fig. 11. No tilt is now present and the disturbance has reached a mature stage. The result is verified by analyses made by Hoem and Hoppestad (1986). The prediction is nearly correct; however, the intensity in the centre of the low might be too weak.

5.2. Shallow disturbances

Within the rest of the cases, more shallow polar low disturbances are present, and the horizontal scale is smaller. In the 3 first cases, there are baroclinic developments directly from the perturbation defined by the shallow warm tongues mentioned earlier.

5.2.1. 29 February–1 March 1984 and 2–4 December 1981. In these two cases, long, warm surface troughs are formed from the initial temperature tongue, and steered southward across the Norwegian Sea. If the disturbance is subtracted from the larger scale northerly flow behind the main cyclone, maximum amplitudes of 7 hPa are found at the sea surface. The model produces a marked occlusion along the trough within a few hours from the start. Fig. 12a shows a 12-hour prediction of the height of the 1000 hPa surface and potential temperature at the lowest sigma level, and Fig. 12b shows 700 hPa height

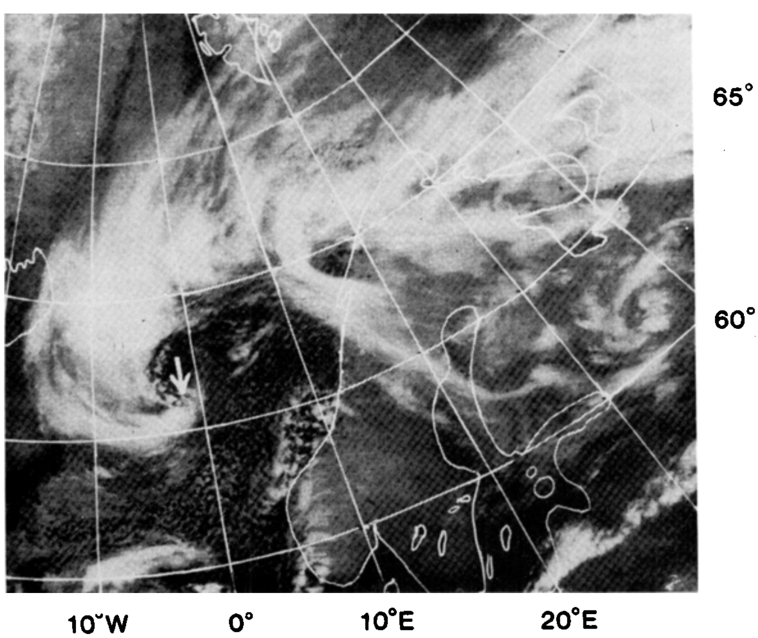

Fig. 10. Infrared satellite picture 0754 GMT 17 December 1982 (Rude Skov, Denmark).

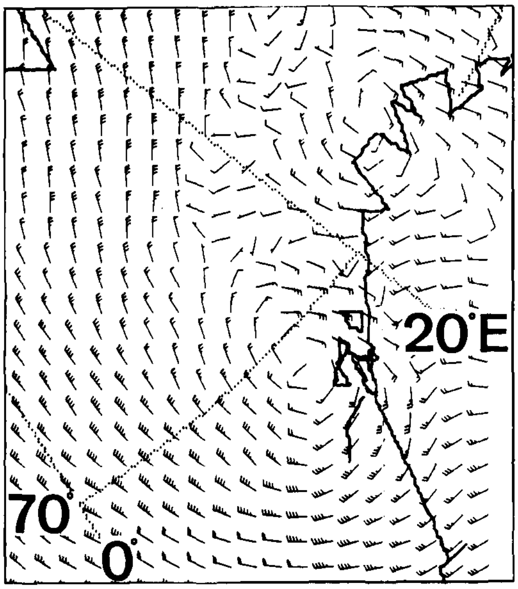

Fig. 11. Prediction 12 GMT 5 March 1984 + 36 hours. Wind at the lowest sigma level. The winds are given in the conventional way.

and potential temperature. At the surface, a sharp, warm trough is present; the tilt of the height disturbance is southward. At 700 hPa, the disturbance is small and more circular in shape. In the following, the trough is sometimes referred to as the warm arm. Its existence is verified by satellite pictures and soundings from weather ship M. Figs. 13 and 14 show the surface prediction after 18 hours together with a verifying surface analyses by Rabbe (1987). At the eastern end of the trough, close to the coast of Norway, the polar low is now developing. A period of rapid growth is estimated to 6 hours.

At the time of the intensification, two cloud clusters with convection are observed, see Fig. 15. The clusters are parallel to each other with a gap with clear sky in between. A similar structure is indicated in the predicted precipitation pattern. A cross-section in direction north-south through the trough after 24 hours is shown in Fig. 16. The occlusion appears as two fronts close to each other. Detailed studies of the vertical velocities and precipitation patterns show vertical circulation in connection with each of the

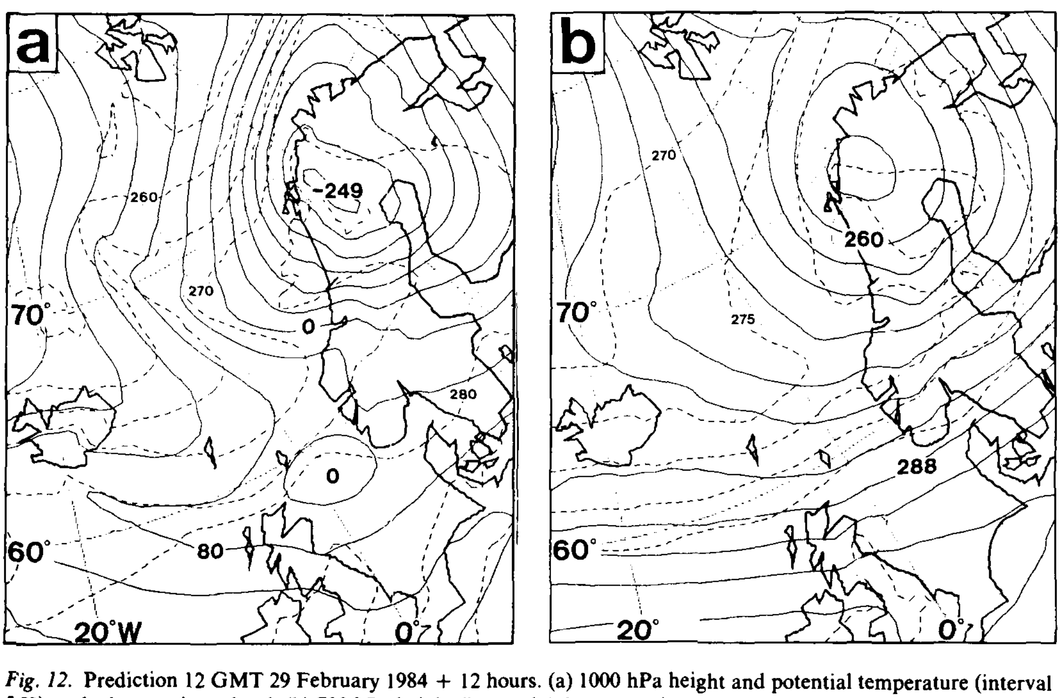

Fig. 12. Prediction 12 GMT 29 February 1984 + 12 hours. (a) 1000 hPa height and potential temperature (interval 5 K) at the lowest sigma level. (b) 700 hPa height (interval 4 decameters) and potential temperature (interval 5 K).

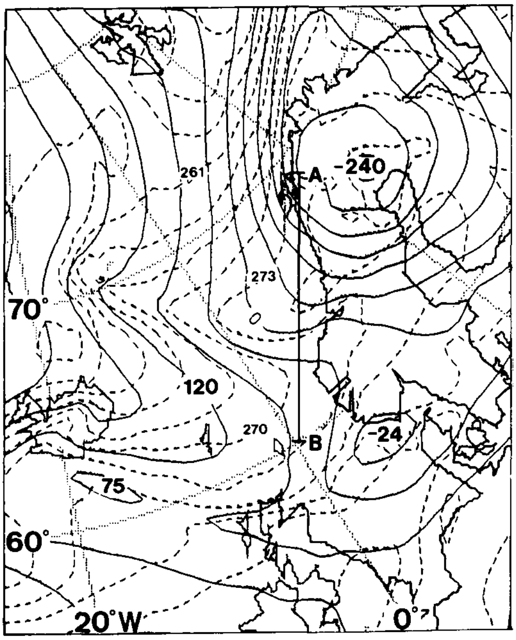

Fig. 13. Prediction of 1000 hPa height and potential temperature (interval 3 K) at the lowest sigma level. 12 GMT 29 February 1984 + 18 hours.

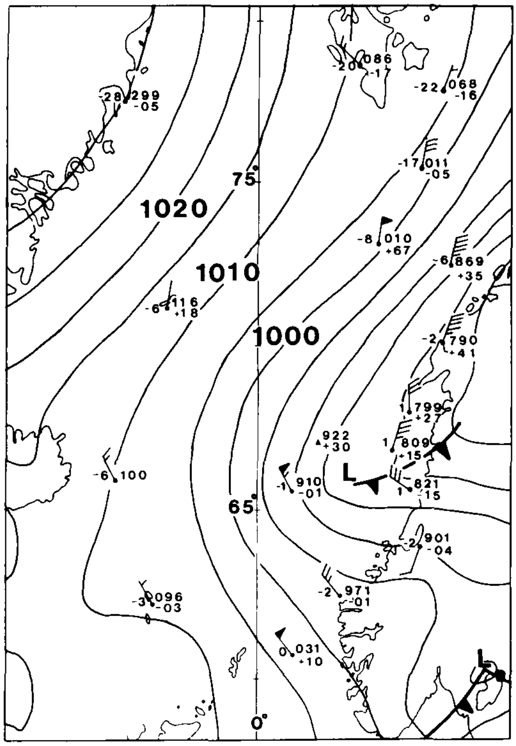

Fig. 14. Surface analysis at 06 GMT 1 March 1984 (Rabbe, 1987).

fronts. Within the warm core, smaller vertical velocities are found; however, no distinct descending motion as might be indicated by the satellite picture is seen.

A few hours later, the surface maps and satellite pictures show a closed circulation. In the model prediction, this intensification is weaker. Maximum surface winds of more than 30 ms^{-1} are observed, while the model winds are about 20 ms^{-1}. The observed minimum surface pressure is 5–10 hPa lower than predicted. Sensitivity experiments show that the baroclinic disturbance is also formed when the release of heat is excluded in the model. However, the intensification of the polar low is significantly stronger when heat fluxes from the ocean and precipitation processes are present. The strongest development is found when parameterization of convection is excluded, but even now the minimum surface pressure is 5 hPa less than observed. Stronger development of the low in this case can be explained from the fact that the released heat is now at lower levels (Bratseth, 1985; Sardie and Warner, 1983).

A similar tongue of warm air is found in the simulations from 2–4 December 1981. Figs. 17a, b shows a 24-hour prediction for 1000 hPa together with the verifying ECMWF analysis. The prediction seems to be accurate.

5.2.2. 19–20 December 1983. Also in this case, the model development is characterized by a shallow, weak baroclinic development directly from a warm tongue in the boundary layer southwest of Spitsbergen. Fig. 18 shows a 36-hour prediction of the wind in the lowest layer. The weak disturbance north of Jan Mayen has a more circular shape than in the two former cases and is even more shallow. A detailed analysis of this situation was made by Hoem (1985). A weak development is found during the next 24 hours. However, further integration does not give larger amplitudes.

5.2.3. 26–27 February 1984. This is the case when the NOAA Arctic Cyclone Expedition made detailed measurements of a polar low (c.f. Shapiro et al., 1987). Their main measurements were taken during a few hours and their analysis

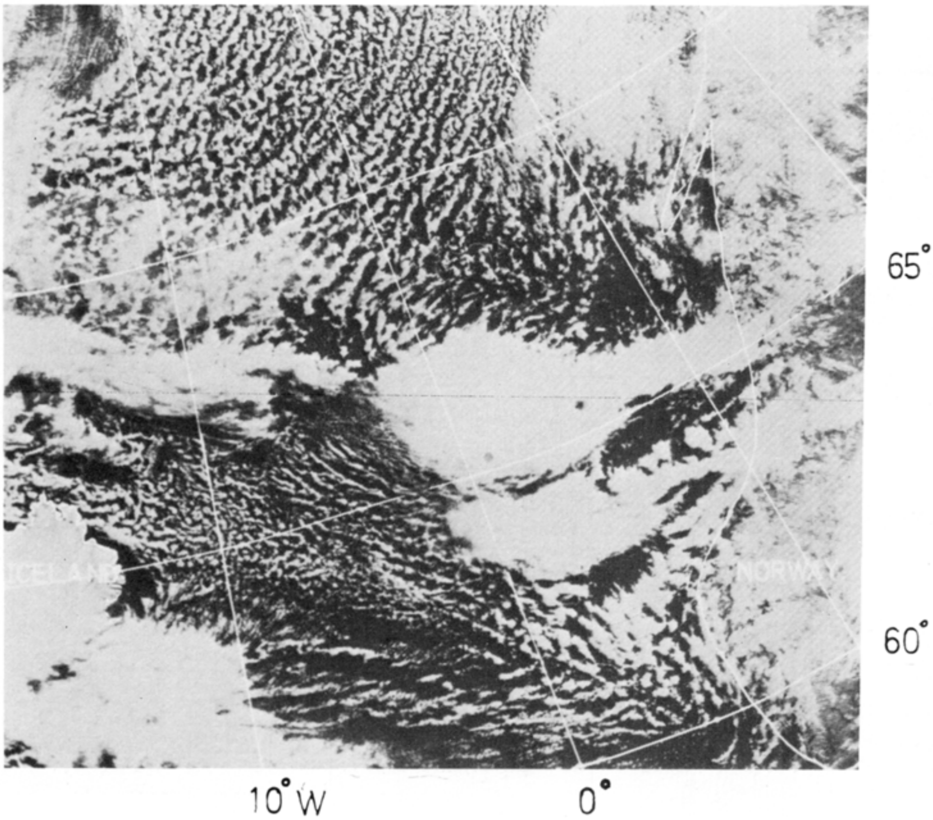

Fig. 15. Infrared satellite picture 0446 GMT 1 March 1984 (Tromsø Telemetri Station, Norway).

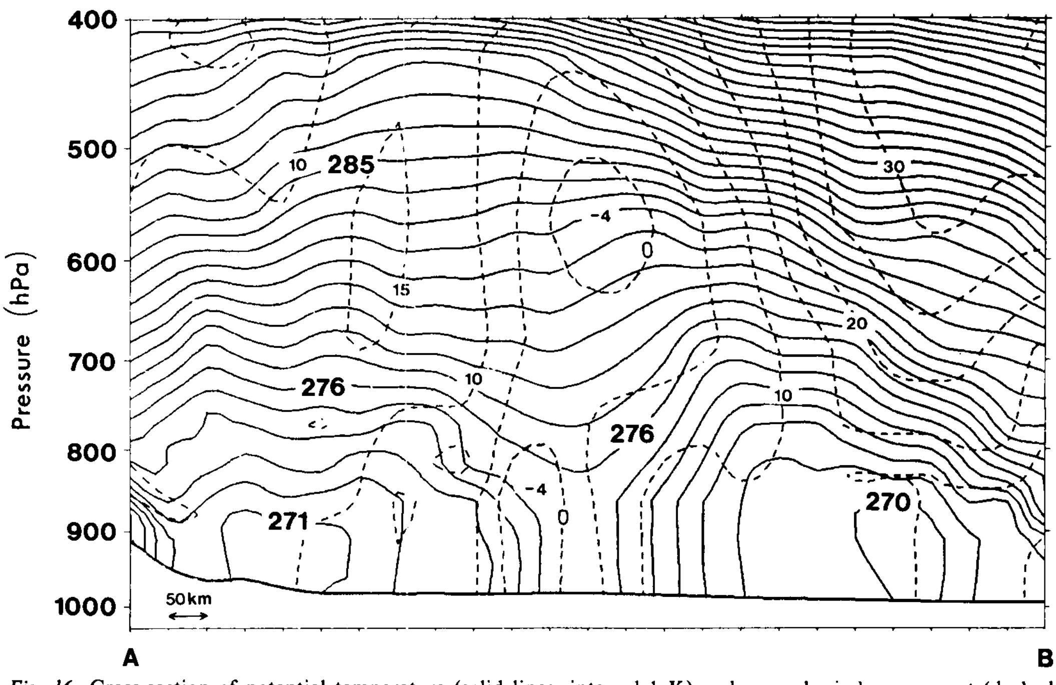

Fig. 16. Cross-section of potential temperature (solid lines, interval 1 K) and normal wind component (dashed lines, interval 5 ms^{-1}). 12 GMT 29 February 1984 + 24 hours. For position, see Fig. 13.

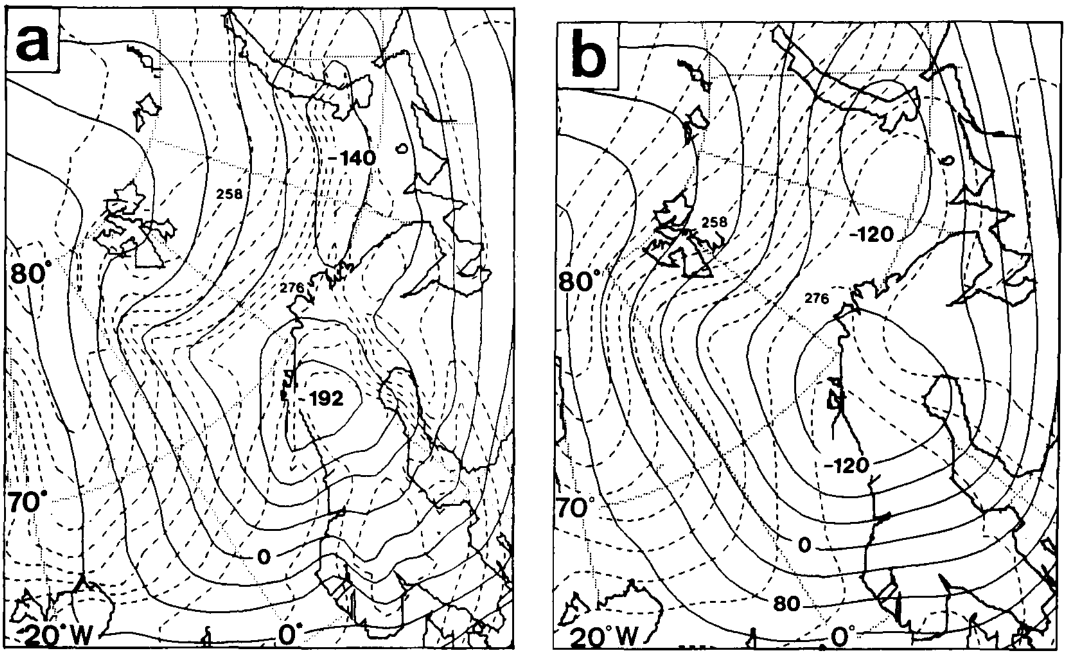

Fig. 17. (a) Prediction of 1000 hPa height and potential temperature (interval 3 K) in the lowest sigma level. 12 GMT 2 December 1981 + 24 hours. (b) ECMWF verifying analysis of 1000 hPa height and potential temperature (interval 3 K), 12 GMT 3 December 1981.

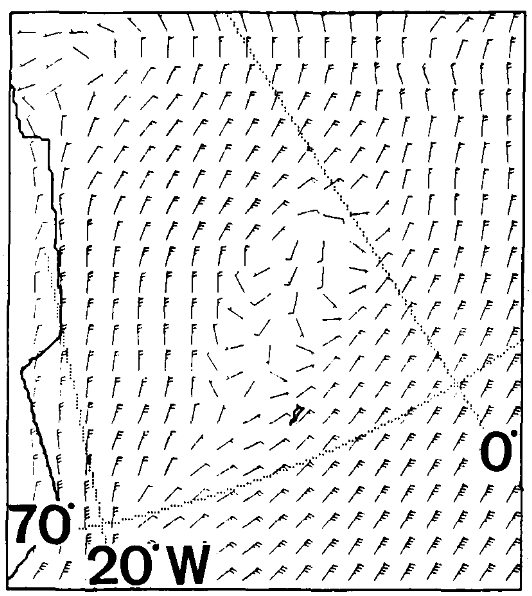

Fig. 18. Prediction 12 GMT 19 December 1983 + 36 hours of wind at the lowest sigma level. The winds are given in the conventional way.

is centred in time to 1340 GMT 27 February, which is approximately 38 hours after the initial time of our simulations. Numerous simulations were made, and detailed results are found in Grønås et al. (1986). Only the main results are given in this paper. The presented figures are from the simulations with 25 km horizontal resolution. The initial and boundary conditions are as described in Section 3.

The formation of the low, as described by our simulations, seems to be complicated. There is no low-level, warm tongue in the initial analysis as in the former cases. However, a cold core above the ice east of Greenland is present in the lower layers. During the first 12 hours of the itegration, a very strong, shallow front is formed along the ice edge, and northerly winds on the western side of the front advect cold air far south along Greenland. East of Iceland a weaker, but deeper cold front, with an orientation from southwest toward northeast, is moving slowly eastward.

The wind and temperature at the lowest sigma layer after 24 hours (6-hour integration with 25 km resolution) is shown in Fig. 19a. Several

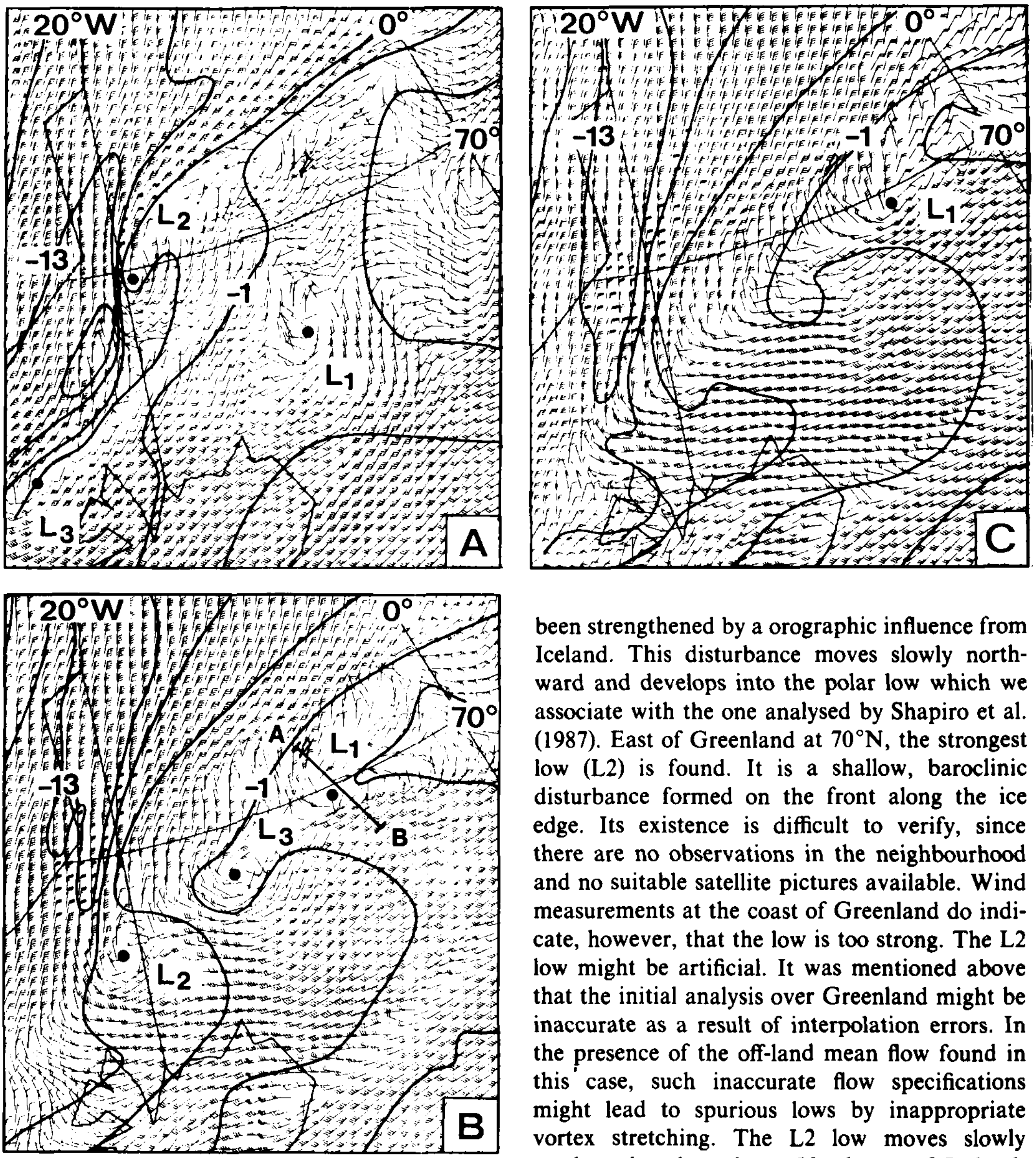

Fig. 19. Predicted wind vectors and temperature (solid lines, interval 4°C) at the lowest sigma level of the 25 km grid model. Initial time is 18 GMT 26 February 1984. (a) 18 GMT + 6 hours. (b) 18 GMT + 18 hours. (c) 18 GMT + 21 hours. The low pressure centres L_1, L_2, L_3 are discussed in the text.

mesoscale disturbances are present. Northeast of Iceland, there is a weak, shallow disturbance (L1), which might be interpreted as a wave on the front moving eastward. This wave might have been strengthened by a orographic influence from Iceland. This disturbance moves slowly northward and develops into the polar low which we associate with the one analysed by Shapiro et al. (1987). East of Greenland at 70°N, the strongest low (L2) is found. It is a shallow, baroclinic disturbance formed on the front along the ice edge. Its existence is difficult to verify, since there are no observations in the neighbourhood and no suitable satellite pictures available. Wind measurements at the coast of Greenland do indicate, however, that the low is too strong. The L2 low might be artificial. It was mentioned above that the initial analysis over Greenland might be inaccurate as a result of interpolation errors. In the presence of the off-land mean flow found in this case, such inaccurate flow specifications might lead to spurious lows by inappropriate vortex stretching. The L2 low moves slowly southward and weakens. Northwest of Iceland, there is a weaker, but deeper low structure (L3) which moves toward the disturbance L1 and weakens.

Fig. 19b shows the wind and temperature after 36 hours (18-hour integration with 25 km resolution). The low L2 is now much weaker and has almost disappeared. The deeper disturbance L3 is approaching L1. Available satellite pictures (Fedor, personal communication) show cloud structures with positions in agreement with the lows L1 and L3. However, the simulation seems to be a few hours too slow. The L3 low is now catching up with the shallow disturbance L1, and 3 hours later in the simulation, the polar low has its maximum intensity (see Fig. 19c). We might interpret the intensification as an upper cold trough catching up with a shallow baroclinic wave, and this is a classical mechanism for strong cyclogenesis (Pettersen, 1962).

The analysis of the polar low by Shapiro et al. (1987) shows a shallow, mesoscale, warm disturbance. The position is ~ 150 km further east southeast than in the simulation. The maximum wind in the boundary layer was measured to 35 ms^{-1}, and the minimum surface pressure is estimated to 980 hPa. The vorticity is estimated to $18f$ southwest of the cyclone. The simulated low (see Fig. 19c) has a horizontal scale of the same size as in the analyses, and a warm core. However, the simulated minimum surface pressure is 992 hPa, and the wind in the boundary layer reaches a maximum of 25 ms^{-1}. The precipitation bands (not shown) are on the northern side as seen on the satellite picture, Fig. 20. The maximum rate of precipitation is 10 mm/6 hours. Maximum vorticity is close to $7f$.

The vertical structure of the forecasted fields as shown by a cross-section of potential and equivalent potential temperature in Fig. 21, has a qualitatively similar warm core and potential instability as in the analysis. Maximum vertical velocities of 1 ms^{-1} are found at 850 hPa a little to the west of the centre of the low. The vertical structure of the simulated low shows some resemblance to a tropical cyclone. However, the pressure perturbations are much smaller and more shallow, and no axial symmetric vortex is found. An eye in the centre of the low is in this case indicated by the analyses and the satellite pictures. For tropical cyclones, the formation of an eye represents a crucial step in the transformation of a disturbance into an intense hurricane (c.f. Anthes, 1982). The surface pressure is then decreased and the circulation is increased. In our simulations, no distinct subsidence is found in the centre of the low. The analysed vertical velocities show narrow bands which cannot be resolved in a model with 25 km grid size.

As in the other cases, the sensitivity experiments give maximum development when the parameterization of convection is excluded in the model. Similar cross-sections as in Fig. 21 are found. The funnel-shaped warm core is now stronger. However, we do not find clear

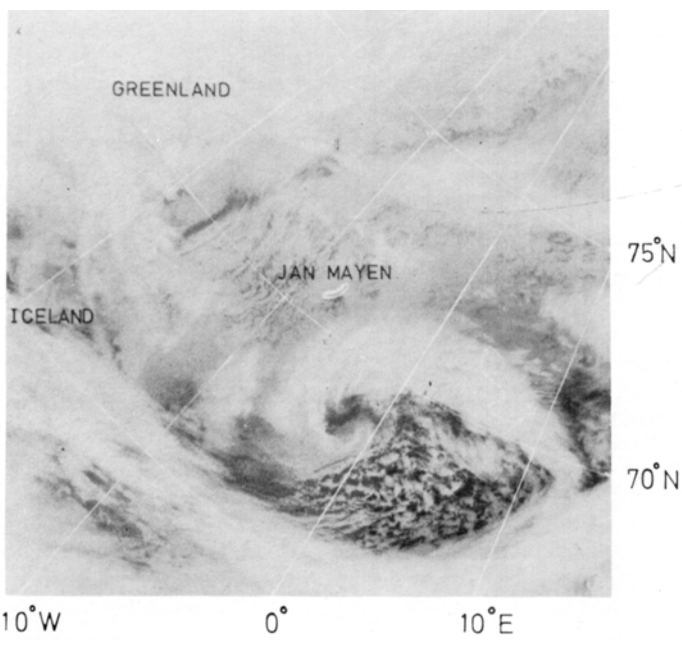

Fig. 20. Infrared satellite picture 1341 GMT 27 February 1984 (University of Dundee, UK).

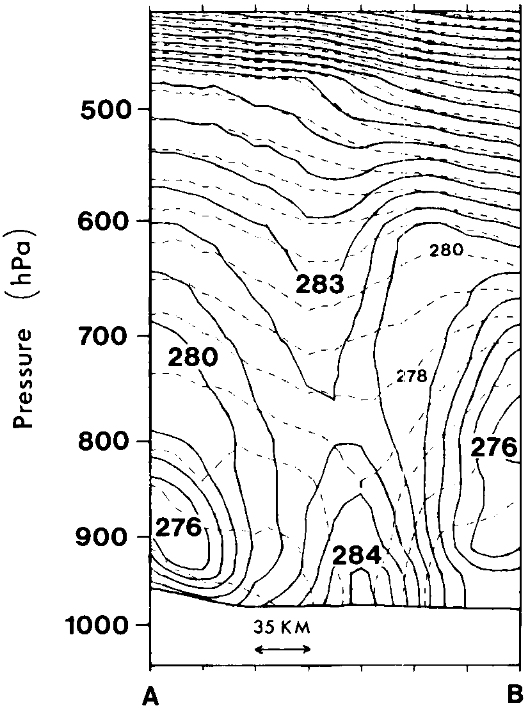

Fig. 21. Predicted N-S cross-section of potential temperature (dashed lines, interval 1°K) and equivalent potential temperature (solid lines, interval 1°K) through the low L_1 after 18 hours, valid at 12 GMT 27 February 1984.

subsidence connected to it, or significantly lower surface pressure than in the presented simulation. The maximum vorticity is close to $8f$ and the maximum rate of precipitation 18 mm/6 hours.

Experiments with a model without parameterization of the precipitation processes demonstrate the importance of the release of latent heat. Without this heating, the predicted disturbances are significantly weaker. However, the main baroclinic development prior to the formation of the intense polar low is found in this case too.

6. Summary

We have used a limited area high resolution NWP model to simulate the development of polar lows in the Norwegian Sea. The model is briefly described together with the initialization procedure. The initial analyses are interpolated from ECMWF operational analyses. The simulations are performed with a horizontal grid distance of 50 km; in one case 25 km resolution is used. In all versions, there were 10 vertical layers. The 50 km model version is integrated both with ECMWF analyses at the lateral boundaries and with prognostic boundary values from the 150 km version of the model. For the 25 km version, the initial state has been a prediction from the 50 km version. The integrations started before any polar low was observed and lasted for 36 or 48 hours.

The initial analyses show cold air in the boundary layer above the ice east of Greenland and a marked temperature gradient toward the warm ocean. In all cases except one, there is a marked tongue of warm air in the boundary layer over the ocean south-west of Spitsbergen. In some of the cases, the development of the polar low is directly connected to this disturbance. The formation of this tongue is connected to differential heating above the sea and the ice, together with the particular shape of the ice edge in the area.

In all cases, disturbances are created which are associated with observed polar lows. The predictions show the polar low disturbance at approximately the right position and time. The errors are, in this respect, more-or-less as in general short-range forecasting. However, we generally fail to predict the strong intensity of the polar lows, especially when the scale of the disturbance is small.

All the simulated polar lows have an initial state where a baroclinic development takes place in a reversed shear flow with northerly winds in the boundary layer. The surface disturbance is warm and conditional vertical instability is connected to it. In this way, the simulated baroclinic development prepares a synoptic situation favourable for some CISK-like mechanism which further develop the low. In two of the cases, a deep baroclinic disturbance is present and polar lows on a relatively large scale are formed. The prediction is here relatively accurate, also with respect to the intensity of the low. In the rest of the cases, the baroclinic disturbances are more shallow, mainly below 700 hPa, and the horizontal scale of the low is smaller. In these cases, the model does not properly handle the rapid growth which follows the initial baroclinic phase. This is probably due to too coarse a resolution or incomplete parameterization of convection. In 3 of the cases, the initial baroclinicity is connected to the warm tongue in the boundary layer southwest of Spitsbergen.

Cross-sections perpendicular to the throughlike surface disturbances show a warm occlusion, or a double-front system. The vertical distribution of potential temperature and equivalent potential temperature (see Fig. 21) show some similarities to the vertical structure of a tropical cyclone. The observed rapid development of a polar low might be connected with locally descending air in the core of the disturbance, which again might cause the intensification of the low with a warm eye. Satellite pictures indeed indicate a warm eye in some of our cases. In our simulations, vertical circulations are generally connected to each branch of the funnel-shaped occlusion. However, no distinct subsidence is found in the core and compared to the measurements, the pressure perturbations are too small. The scale of the analysed vertical circulations made by Shapiro et al. (1987), indicates that the resolution of the model has to be increased in order to properly simulate the rapid intensification of a polar low.

Sensitivity experiments demonstrate the importance of heating from the ocean and precipitation processes for the formation of polar lows. The baroclinic initial phase of the development is also simulated in a model where these processes are excluded. However, the development is significantly weaker. In particular, the circulations connected with the occlusions are weaker. Parameterization of convection seems to be important. The strongest development is found when latent heat is released at relatively low levels. When the horizontal resolution is increased from 50 to 25 km grid distance, the mesoscale features are better defined. However, the differences between the simulations are small compared to the deviations from the measurements. When analyses are used as lateral boundary conditions, the positioning of the lows are always improved.

Our results give some indications of how well polar lows might be forecasted with a mesoscale numerical model. It is very promising that the ECMWF synoptic-scale initial analyses seem to describe in necessary detail the essential features from which the polar lows are formed. The low-level cold air above the ice is well described and so is the warm boundary layer over the ocean. The high quality of the analyses cannot alone be explained from the distribution and frequency of observations in the area. The model used in the ECMWF assimilation process seems to be able to transform air masses over ice and ocean, and in this way contribute to the high quality. In this study, we have investigated cases when polar lows did occur. In an operational routine with our model, the baroclinic initial phase will probably be predicted both in cases when intense polar lows are formed and when no intensification is found; prediction of the intensification of polar lows will still be difficult.

7. Acknowledgements

This work has been performed as a subtask of the Polar Lows Project which was partly financed by the oil companies with licences north of 62° N on the Norwegian continental shelf. The authors wish to express their gratitude to their colleagues, Mr. Vebjørn Hoem, Mr. Knut Helge Midtbø and Dr. Thor Erik Nordeng at the Norwegian Meteorological Institute, for valuable discussions and technical assistance. We also wish to thank Professor Hans Økland and Dr. Arne Bratseth for helpful conversations concerning the numerical methods and the results of the simulations. The results from one of the simulations, 27 February 1984, have been thoroughly discussed with Dr. Melvin Shapiro, and we are grateful for his advice.

REFERENCES

Anthes, R. A. and Warner, T. T. 1978. Development of hydrodynamic models suitable for air pollution and other mesometeorological studies. *Mon. Wea. Rev. 106*, 1045–1078.

Anthes, R. A. 1982. Tropical cyclones. Their evolution, structure and effects. *Meteorol. Monorg. 19*, American Meteorological Society.

Bratseth, A. 1982. A simple and efficient approach to the initialization of weather prediction models. *Tellus 34*, 352–357.

Bratseth, A. 1983. Some economical, explicit finite-difference schemes for the primitive equations. *Mon. Wea. Rev. 111*, 663–668.

Bratseth, A. 1985. A note on CISK in polar air masses. *Tellus 37A*, 403–406.

Brown, J. A. and Campana, K. A. 1978. An economical time-differencing system for numerical weather prediction. *Mon. Wea. Rev. 106*, 1125–1136

Davies, H. C. 1976. A lateral boundary formulation for multilevel prediction models. *Q. J. R. Meteorol. Soc. 102*, 405–418.

Duncan, C. N. 1977. A numerical investigation of polar lows. *Q. J. R. Meteorol. Soc. 103*, 255–268.

Duncan, C. N. 1978. Baroclinic instability in a reversed shear flow. *Meteorol. Mag. 107*, 17–23.

Grønås, S. and Hellevik, O. E. 1982. *A limited area prediction model at the Norwegian Meteorological Institute.* Techn. Rep. No. 61, The Norwegian Meteorological Institute, Oslo, Norway.

Grønås, S., Foss, A. and Lystad, M. 1986. *Numerical simulations of polar lows in the Norwegian Sea. Part I: The model and simulations of the polar low 26–27 February 1984.* Polar Lows Project. Technical Report No. 5. The Norwegian Meteorological Institute, Oslo, Norway.

Grønås, S. and Midtbø, K. H. 1986. *Four-dimensional data assimilation at the Norwegian Meteorological Institute.* Techn. Rep. No. 66, The Norwegian Meteorological Institute, Oslo, Norway.

Harrold, T. W. and Browning, K. A. 1969. The polar low as a baroclinic disturbance. *Q. J. R. Meteorol. Soc. 95*, 710–723.

Haugen, J. E. (1986). Numerical simulations with an idealized model. *Proceedings of the International Conference on Polar Lows.* Oslo, Norway, 20–23 May 1986. The Norwegian Meteorological Institute, Oslo, Norway.

Hoem, V., Hoppestad, S. and Rabbe, Å. 1984. *Polar low case studies. I. December 1982–December 1985.* Techn. rep. no. 3, Polar Lows Project, The Norwegian Meteorological Institute, Oslo, Norway

Hoem, V. 1985. *Polar low case studies II 1982–85.* Techn. rep. no. 6, Polar Lows Project, The Norwegian Meteorological Institute, Oslo, Norway

Hoem, V. and Hoppestad, S. 1986. *Polar low case studies III 1982–1985.* Techn. rep. no. 12, Polar Lows Project, The Norwegian Meteorological Institute, Oslo, Norway.

Hoskins, B. J. and Bretherton, F. P. 1972. Atmospheric Frontogenesis Models. Mathematical Formulation and Solution. *J. Atmos. Sci. 29*, 11–37.

Janjic, Z. 1977. Pressure gradient force and advection scheme used for forcasting with steep and small scale topography. *Beitr. Phys. Atmos. 50*, 186–199.

Kristoffersen, D. R. 1985. *Polar lows observed during winter 1983/84 in the adjacent seas of Norway.* Tech rep. no. 9, Polar Lows Project, The Norwegian Meteorological Institute, Oslo, Norway.

Källberg, P. 1977. *Test of a lateral boundary relaxation scheme.* ECMWF Research Department, Internal Report No 3, Febr. 1977.

Louis, J-F. 1979. A parametric model of vertical eddy fluxes in the atmosphere. *Boundary Layer Meteorol. 17*, 187–202.

Mansfield, D. A. 1974. Polar lows: The development of baroclinic disturbances in cold air outbreaks. *Q. J. R. Meteorol. Soc. 100*, 541–544.

Mesinger, F. and Arakawa, A. 1976. *Numerical methods used in atmospheric models.* GARP Publ. Ser., No. 17, WMO, Geneva, 64 pp.

Nordeng, T. E. 1986. *Parameterization of physical processes in a three dimensional numerical weather prediction model.* Techn. Rep. No. 65, The Norwegian Meteorological Institute, Oslo, Norway.

Økland, H. 1976. *An example of air-mass transformation in the arctic and connected disturbances of the wind field.* Report DM-20 Department of Meteorology, University of Stockholm, Sweden.

Økland, H. 1977. *On the intensification of small-scale cyclones formed in very cold air masses heated by the ocean.* Institute report series No. 26. Department of Geophysics, University of Oslo, Norway.

Økland, H. 1978. *On formation of fronts by differential heating of the atmosphere.* Institute report series No. 38. Department of Geophysics, University of Oslo, Norway.

Pettersen, S., Bradbury, D. L. and Pedersen, K. 1962. The Norwegian cyclone models in relation to heat and cold sources. *Geophysica Norvegica 24.* Special Issue in memory of Vilhelm Bjerknes on the 100th anniversary of his birth.

Rabbe, Å. 1987. A Polar Low over the Norwegian Sea, 29 February-1 March 1984. *Tellus 39A*, 326–333.

Rasmussen, E. 1979. The polar low as an extratropical CISK-disturbance. *Q. J. R. Meteorol. Soc. 105*, 531–549.

Rasmussen, E. 1981. An investigation of a polar low with a spiral cloud structure. *J. Atmos. Sci. 38*, 1785–1792.

Rasmussen, E. 1985. *A polar low development over the Barents sea.* Techn. rep. no. 7, Polar Lows Project, the Norwegian Meteorological Institute, Oslo, Norway.

Sardie, J. M. and Warner, T. T. 1983. On the mechanism for the development of polar lows. *J. Atmos. Sci. 40*, 869–881.

Sardie, J. M. and Warner, T. T. 1985. A numerical study of the development mechanism of polar lows. *Tellus 37A*, 460–477.

Seaman, N. L., Otten, H. and Anthes, R. A. 1982. *A rapid developing polar low in the North Sea on 2 January 1979.* Preprint Volume, First Intern. Conference on Met. and Air/Sea Interaction of the Coastal Zone, The Hague, Netherland.

Shapiro, R. 1970. Smoothing, filtering, and boundary effects. *Rev. Geophys. Space Phys. 8*, 359–387.

Shapiro, M. et al. (1987), personal communication.

Wilhelmsen, K. 1985. Climatological study of gale-producing polar lows near Norway. *Tellus 37A*, 451–459.

Wilhelmsen, K. 1986. *Climatological study of polar lows near Norway.* Part I. Techn. rep. no. 4, Polar Lows Project, The Norwegian Meteorological Institute, Oslo, Norway.